

# 1    **Anthropogenically forced shift in ENSO mean state after 1970 CE**

2            Paul S. Wilcox<sup>1\*</sup>, Manfred Mudelsee<sup>2</sup>, Christoph Spötl<sup>1</sup>, R. Lawrence Edwards<sup>3</sup>

3            <sup>1</sup>Institute of Geology, University of Innsbruck, 6020 Innsbruck, Austria

4            <sup>2</sup>Climate Risk Analysis, Kreuzstrasse 27, Heckenbeck, 37581 Bad Gandersheim, Germany

5            <sup>3</sup>Department of Earth Sciences, University of Minnesota, Minneapolis, MN, 55455, USA

6            \*Corresponding author: paul.wilcox@uibk.ac.at

7            Keywords: ENSO, North Pacific, Anthropocene, Speleothems

## 8    **Abstract**

9    Understanding how El Niño-Southern Oscillation (ENSO) responds to natural variability is of  
10    key importance for future climate projections under a warming climate. However, there is no  
11    clear consensus on what drives ENSO's variability on centennial timescales. Here, we find  
12    that the epikarst in southeastern Alaska is effective at filtering ENSO and solar irradiance  
13    signals from the Aleutian Low regional climate, which are subsequently recorded in the  
14    speleothem proxy data. By applying a correlation test, we find that ENSO was significantly  
15    influenced by solar irradiance over the past ~3,500 years. This relationship dissolved after  
16    ~1970 CE, with ENSO now being dominated by anthropogenic forcing. This implies a new  
17    ENSO mean state that will need to be incorporated into future climate projections.

18

19

20

21

## 22    **Introduction**

23            El Niño-Southern Oscillation (ENSO) is an important driver of Earth's climate  
24    (McPhaden et al., 2006, Deser et al., 2010), fluctuating with significant variability between El  
25    Niño (warm phase) and La Niña (cold phase). Instrumental records, only available for the  
26    past 150 years, are too short to fully capture ENSO variability on centennial timescales  
27    (Stevenson et al., 2012). Paleoclimate proxy techniques attempt to fill this gap by providing  
28    ENSO records extending deeper in time. However, these records generally either cover the  
29    past few centuries only, lack high temporal resolution, or cover non-continuous intervals of  
30    the past millennium.

31            One of the main uncertainties associated with ENSO variability is the influence of  
32    solar forcing. It has been hypothesized that an ocean thermostat response of the tropical  
33    Pacific to solar forcing induces both La Niña and El Niño mean states (Clement et al., 1996,  
34    Emile-Geay et al., 2007). This hypothesis has found some support in central Pacific corals  
35    (Cobb et al., 2003), North American tree rings documenting medieval megadroughts (Cook et  
36    al., 2004), and multiproxy climate field reconstructions (Mann et al., 2009). In each of these  
37    cases, however, unambiguous confirmation of solar forcing is lacking. This has led some  
38    studies to suggest an insignificant response of ENSO to solar forcing, with internal variability  
39    being the main driver of ENSO variations (Cobb et al., 2013). Given the recent rise in  
40    anthropogenic warming over the past several decades, it becomes increasingly important to  
41    understand the full natural range of ENSO variability and its underlying forcing for  
42    improving future climate projections.

43            The North Pacific provides an ideal location to examine ENSO variability through a  
44    well-known atmospheric bridge, which links equatorial Pacific and North Pacific climate  
45    variability (Liu & Alexander, 2007; Diaz et al., 2001; Alexander et al., 2002) (Fig. 1,

Supplementary Fig. S1). The Aleutian Low is the principal climate feature in southeastern Alaska that is influenced by this atmospheric bridge (Alexander et al., 2002; Bjerknes, 1966; Bjerknes, 1969), and steers storms and abundant precipitation into the region, especially when strengthened. In general, the link between the equatorial Pacific and the North Pacific is expressed as a stronger-than-normal Aleutian Low during warm sea surface temperature anomalies in the equatorial Pacific (i.e. El Niño), and weaker-than-normal Aleutian Low during cool sea surface temperature anomalies (i.e. La Niña) (Alexander et al., 2002; Bjerknes, 1966; Bjerknes, 1969). Sea-surface temperatures in the equatorial Pacific, in turn, may be influenced by solar irradiance (Clement et al., 1996, Emile-Geay et al., 2007), which would impact the mean-state of ENSO (Clement et al., 1996, Emile-Geay et al., 2007), and consequently affect the strength of the Aleutian Low via the atmospheric bridge. It has been shown that stronger solar irradiance is generally associated with a weaker Aleutian Low while weaker solar irradiance is associated with a stronger Aleutian Low (Osterberg et al., 2014). Therefore, there is a known link between both solar irradiance and ENSO and the strength of the Aleutian Low, typically on decadal timescales.

Based on these known links between the equatorial Pacific and the North Pacific, we hypothesize that solar irradiance forces ENSO mean state changes which, in turn, force the strength of the Aleutian Low via the atmospheric bridge. In other words, decreased solar irradiance should correspond to an increased frequency of El Niño events and result in an overall strengthened Aleutian Low. Conversely, increased solar irradiance should correspond to an increased frequency of La Niña events and result in an overall weakening of the Aleutian Low. This hypothesis would be in agreement with the ocean thermostat mechanism (Clement et al., 1996, Emile-Geay et al., 2007).

Speleothems, which provide long-term reconstructions of climate in the region (Wilcox et al., 2019), offer an untested approach to record Aleutian Low, and hence

71 ENSO/solar irradiance, responses in the North Pacific. Here, we utilize speleothems from  
72 southeastern Alaska to generate a high-resolution and precisely dated record spanning  
73 continuously the past ~3,500 years. Our data demonstrate that the local epikarst in  
74 southeastern Alaska is effective at filtering ENSO and solar irradiance signals from the  
75 Aleutian Low regional climate. From this, we find that solar forcing has been the primary  
76 driver of ENSO variability on centennial timescales, and that this relationship dissolved at  
77 ~1970, likely due to anthropogenic forcing.

## 78 **Results**

### 79 **Site location and speleothems**

80 Our datasets were developed from two stalagmites retrieved in spring/summer 2021 in  
81 two caves on Prince of Wales Island, located in the temperate rainforest of the southern  
82 Alexander Archipelago in Alaska. Klawock, the nearest village to the caves (Supplementary  
83 Fig. S2), has a mean annual air temperature of 7.4 °C and receives ~300 mm of precipitation  
84 annually. Speleothem WB-21-5-A is 536 mm in length and was found 50 m inside Wishbone  
85 Cave (55.776° N, 133.195° W; 350 m a.s.l.), and WA-21-6-A is 181.5 mm in length and was  
86 found 100 m inside Walkabout Cave (55.774 N, -133.191 W; 420 m a.s.l.) (Supplementary  
87 Fig. S3). Interior cave temperatures are a constant 5.6 °C for Walkabout Cave, and vary  
88 between 2.5 and 8.6 °C for Wishbone Cave (Supplementary Fig. S4). Both speleothems were  
89 actively dripping during recovery, suggesting that the speleothem tops are modern. There are  
90 no visually detectable hiatuses, and growth rates are constant for both speleothems  
91 (Supplementary Fig. S5). Speleothems WB-21-5-A and WA-21-6-A were sampled for  $\delta^{18}\text{O}$   
92 and  $\delta^{13}\text{C}$  at 0.5 mm and 0.25 mm resolution, respectively, producing a temporal resolution of  
93 ~2–5 years for both speleothems. Additionally, speleothem WB-21-5-A was sampled for  
94 fluid inclusion  $\delta\text{D}$  every 0.5 cm, producing a temperature record with a resolution of ~40  
95 years (Supplementary Fig. S6).

## 96 Controls on speleothem $\delta^{18}\text{O}$

97       The amount effect is likely the dominant control on  $\delta^{18}\text{O}$  in precipitation at the cave  
98 sites whereby higher rainfall amounts results in more depleted  $\delta^{18}\text{O}$  values (Dansgaard,  
99 1964), as indicated by a regional comparison of modern precipitation (Supplementary Fig.  
100 S7). We can reasonably exclude both topographic barriers and changing source regions as  
101 dominant controls on  $\delta^{18}\text{O}$  in precipitation as there are no topographic barriers between the  
102 cave sites and the Pacific Ocean to cause isotopic depletion, and precipitation in the region is  
103 dominantly sourced from the Pacific Ocean (Bailey et al., 2019). Further, there is a weak  
104 relationship between changes in air temperature and  $\delta^{18}\text{O}$  of precipitation in southcentral  
105 Alaska, with surface air temperatures explaining only ~30% of variability in the  $\delta^{18}\text{O}$   
106 precipitation data (Bailey et al., 2019). Although there are no isotope in precipitation  
107 monitoring networks in southeastern Alaska, the region as a whole is strongly influenced by  
108 the Aleutian Low (Bailey et al., 2019) and likely has a similar weak relationship between air  
109 temperature and  $\delta^{18}\text{O}$  of precipitation. Therefore, we argue that  $\delta^{18}\text{O}$  of calcite is dominantly  
110 controlled by the amount of precipitation, with depleted isotope values indicating more  
111 precipitation, and vice versa. This is corroborated by drip rate data from the site of  
112 speleothem WA-21-6-A, which closely mirror local precipitation amount (Supplementary  
113 Fig. S4).

114       The amount effect controlling  $\delta^{18}\text{O}$  in precipitation at the cave sites implies that  
115 speleothem oxygen isotopes are a reliable proxy to determine the strength of the Aleutian  
116 Low. Depleted speleothem  $\delta^{18}\text{O}$  indicates a strengthened Aleutian Low, and vice versa,  
117 consistent with regional lake proxy data (Anderson et al., 2005) and ice core data (Osterberg  
118 et al., 2014). To test if ENSO and solar irradiance signals can be extracted from speleothem  
119  $\delta^{18}\text{O}$ , we applied the binned correlation coefficient ( $r$ ) to find reliable statistical linkages  
120 among pairs of proxy data on unequal timescales (Mudelsee, 2014) (see methods for details

on the statistics). First, we examine correlations between speleothem data, and then apply the correlation test with solar irradiance and ENSO proxy data.

### Speleothem proxy correlations

For speleothem WB-21-5-A, we find that the fluid inclusion temperature reconstruction correlates significantly with  $\delta^{18}\text{O}$  at  $r = 0.59$  with a 90% calibrated bootstrap confidence interval of [0.43; 0.71] (Supplementary Fig. S8). If we examine between sites, the  $\delta^{18}\text{O}$  series from speleothems WA-21-6-A and WB-21-5-A are significantly correlative,  $r = 0.25$  [0.01; 0.45] (Supplementary Fig. S8), highlighting regional consistencies that would be expected between neighboring speleothem  $\delta^{18}\text{O}$  data that precipitated close to isotopic equilibrium with the drip water (Supplementary Fig. S9). We argue that deviations between speleothem  $\delta^{18}\text{O}$  are a result of spectral frequency differences between sites (Fig. 2), with speleothem WB-21-5-A recording a high-frequency  $\delta^{18}\text{O}$  signal and WA-21-6-A recording a low-frequency  $\delta^{18}\text{O}$  signal (Supplementary Fig. S10). This is likely the result of the large difference in growth rate (Supplementary Fig. S5), and hence drip rate, between the two sites. Since drip water transports the  $\delta^{18}\text{O}$  signal from the soil zone to the speleothem site, different drip rates will lead to different  $\delta^{18}\text{O}$  frequencies at each speleothem site. We hypothesize that the regional epikarst acts as a low-pass filter, resulting in a modulation of the Aleutian Low regional climate signal (Fig. 3). In speleothem WA-21-6-A, we observe a climate signal that is potentially linked with total solar irradiance (TSI), while in speleothem WB-21-5-A, we observe a climate signal that is potentially linked with ENSO. We then explore the statistical significance of these potential climate linkages to determine if they are robust.

### Solar irradiance and ENSO correlations

To determine if the  $\delta^{18}\text{O}$  series from speleothem WA-21-6-A is statistically linked with TSI, we compared the  $\delta^{18}\text{O}$  proxy to the most up-to-date physics-based reconstruction of

TSI currently available (Wu et al., 2018) (Fig. 4). We find that TSI correlates significantly with speleothem WA-21-6-A  $\delta^{18}\text{O}$  after  $\sim 0$  CE at  $r = 0.52$  [0.32; 0.68] (Supplementary Fig. S8), with decreased solar irradiance correlating with a strengthened Aleutian Low in speleothem WA-21-6-A, and vice versa for increased solar irradiance. However, we find no significant correlation prior to  $\sim 0$  CE. The lack of correlation for the earlier part could be due to proxy bias, with all previous TSI reconstructions dependent on  $^{14}\text{C}$  and  $^{10}\text{Be}$  data. Additionally, we performed a spectral analysis, which shows solar cycles (Moussas et al., 2005) at all 3 spectral peaks of 16-, 19-, and 28-year periods (Fig. 2), providing enhanced confidence that speleothem WA-21-6-A reliably records TSI variability. However, due to the lack of correlation prior to  $\sim 0$  CE, we only provide interpretations for the past  $\sim 2000$  years.

To determine if the  $\delta^{18}\text{O}$  series from speleothem WB-21-5-A is statistically linked with ENSO, we compared the  $\delta^{18}\text{O}$  proxy to an ENSO reconstruction produced from a coral  $\delta^{18}\text{O}$  record in the central tropical Pacific spanning the past  $\sim 750$  years (23) (Fig. 4). We find that the coral  $\delta^{18}\text{O}$  (Dee et al., 2020) is significantly correlated with speleothem WB-21-5-A at  $r = 0.54$  [0.10; 0.80] (Supplementary Fig. S8), with increased frequency of El Niño events correlating with a strengthened Aleutian Low in speleothem WB-21-5-A, and vice versa for La Niña events (Fig. 4). Additionally, we performed a spectral analysis, which shows the “classical” ENSO power (Allen, 2000) at the 7.2-year period (Fig. 2), which is added confidence that speleothem WB-21-5-A reliably records ENSO variability.

The correlation tests confirm that the strength of the Aleutian Low correlates significantly with either solar irradiance or ENSO. And, since speleothem WA-21-6-A  $\delta^{18}\text{O}$  (solar irradiance signal) and WB-21-5-A  $\delta^{18}\text{O}$  (ENSO signal) are significantly correlated, this provides compelling evidence that solar irradiance can influence ENSO mean state changes. More specifically, it agrees with our hypothesis that solar irradiance forces ENSO mean state changes which, in turn, force the strength of the Aleutian Low via the atmospheric bridge

(Fig. 3). Our data thus supports the ocean thermostat mechanism (Clement et al., 1996, Emile-Geay et al., 2007) before 1970 CE. After 1970 CE, ENSO deviates from natural variability based on the lack of correlation between temperature and precipitation (Fig. 3)

## Discussion

Our data shows that solar forcing can have an influence on ENSO mean state changes on centennial timescales over the past ~3,500 years. Notably, this confirms the ocean thermostat mechanism whereby solar irradiance induces changes in the east-west temperature gradient of the tropical Pacific and, hence, ENSO activity (Clement et al., 1996, Emile-Geay et al., 2007). In general, periods of increased solar irradiance correspond to an increase frequency of La Niña events, while decreased solar irradiance corresponds to an increase frequency of El Niño events (Fig. 4).

In southeastern Alaska, warm/dry conditions correspond to La Niña mean states and cool/wet conditions correspond to El Niño mean states. Regional glacial retreats/advances follow this trend (Supplementary Fig. S11) (Wiles et al., 2008). Only the El Niño mean state change at ~500 CE does not fully agree with solar irradiance (Fig. 4), and may be associated with the strongest volcanic eruption in the past 2,500 years (Sigl et al., 2015). This event is in conjunction with one of the most extensive regional glacial advances in the past 2000 years (Sigl et al., 2015), and may correspond to the Late Antique Little Ice Age (LALIA), whereby unprecedented summer cooling is recorded by tree rings in Europe (Büntgen et al., 2016). Therefore, we find that ENSO mean state changes are mostly insensitive to volcanic eruptions, consistent with coral reconstructions (Dee et al., 2020), except for exceedingly rare super-eruptions such as the ~500 CE eruption.

Atmospheric CO<sub>2</sub> strongly disconnects from the natural variability of the speleothem record after ~1850 CE (Supplementary Fig. S12), in agreement with the rise of CO<sub>2</sub> above



pre-industrial levels (Ahn et al., 2012). This is notable, given that the equatorial Pacific represents the largest CO<sub>2</sub> source globally (Takahashi et al., 2009), and is clearly at odds with natural forcings indicated by the speleothem record. Given the insignificant increase in solar irradiance to such a remarkable rise in atmospheric CO<sub>2</sub>, it is obvious that anthropogenic greenhouse gases are responsible for the deviation from natural variability. We suggest that this resulted in the breakdown of the ocean thermostat mechanism in the 1970s, in conjunction with a well-documented ENSO and North Pacific regime shifts in the late 1970s (Diaz et al., 2001, Hare & Mantua, 2001; Giamalaki et al., 2018; Mayo & March, 1990; Graham, 1994). This has resulted in increasingly warmer/wetter conditions in southeast Alaska unseen during the previous ~3,500 years. The warm/wet combination is inconsistent with previous regional El Niño or La Niña mean-state responses, and indicates a significant change in ENSO properties (Graham, 1994; Freund et al., 2019; Wang et al., 2019).

While the regime shifts in the late 1970s could also be attributed to a disruption in the atmospheric bridge linking the equatorial Pacific to the North Pacific, we argue that this is unlikely given the significant correlation between modern-day instrumental records of ENSO and regional southeastern Alaska precipitation/temperature (Supplementary Fig. S1). This implies that the atmospheric bridge is still strong, with ENSO continuing to force the strength of the Aleutian Low even under increased greenhouse gases.

We suggest that a switch to the weaker Walker mechanism in the 1970s, whereby zonal tropical sea-surface temperatures are reduced (Vecchi et al., 2008), resulted in the mean state shift of ENSO. Based on our speleothem data, the switch to a weaker Walker mechanism in the 1970s would not be possible if driven by natural forcings alone, and required the input of anthropogenic greenhouse gases. Reduced zonal tropical sea-surface temperatures has led to an El Niño mean-state and a strengthened Aleutian Low, but with regional atmospheric warming that is more typical of a La Niña mean-state. This significant

change in ENSO may suggest that a climate change tipping point may have been crossed in the 1970's. We recommend that climate models fix biases that will result in both a diminished ocean thermostat response and an increased weaker Walker response at ~1970 CE for improved climate projections of ENSO.

## **Materials and Methods**

Speleothems WA-21-6-A and WB-21-5-A were cut in half and polished, with total lengths measured at 181.5 and 536 mm, respectively. Lengths were measured relative to the central growth axis. The base of the speleothems begins at 0 mm. "Hendy" tests (Hendy, 1971) were performed at four different locations at 2.3, 6.5, 9.9, and 15 cm in WA-21-6-A, and five different locations at 4, 13.8, 25.6, 37.1, and 48 cm in WB-21-5-A to test for isotope equilibrium fractionation (Supplementary Fig. S9). Fabric texture was identified visually, and shows consistent fabric throughout speleothems, with no evidence of hiatuses.

### **U-Th ages**

A total of 10 powdered calcite samples were manually drilled for U-Th dating under a laminar flow hood; 5 from WA-21-6-A, and 5 from WB-21-5-A (Supplementary Fig. S3, <https://doi.pangaea.de/10.1594/PANGAEA.949778>). U-Th samples were processed at the University of Minnesota Trace Metal Isotope Geochemistry Lab and analysed using a ThermoFisher Neptune Plus multi-collector inductively coupled plasma mass spectrometer equipped with an Aridus desolvation nebulizer, following the method of (Shen et al., 2012). Ages are reported with  $2\sigma$  errors in BCE/CE. A time-depth model was created in OxCal 4.4 using the Bayesian approach (Bronk Ramsey, 2008; Bronk Ramsey, 2009; Bronk Ramsey & Lee, 2013).

## Stable isotopes

A total of 1800 stable isotopes locations were drilled using a Merchantek micromill. In WA-21-6-A, samples were drilled every 0.25 mm, yielding a temporal resolution of ~5 years. Samples in WB-21-5-A were drilled every 0.5 mm, yielding a temporal resolution of ~2-5 years. Stable isotope samples were analysed at the University of Innsbruck using a ThermoFisher Delta V isotope ratio mass spectrometer equipped with a Gasbench II (Spötl, 2011). Stable isotopes are reported in per mil relative to Vienna Pee Dee Belemnite (VPDB). Long-term analytical precision is less than or equal to 0.08‰ for both  $\delta^{13}\text{C}$  and  $\delta^{18}\text{O}$  ( $1\sigma$ ).

## Fluid inclusions

Speleothem fluid inclusion water isotopes were analysed at the University of Innsbruck using continuous-flow technique of water via high-temperature reduction on glassy carbon (Dublyansky & Spötl, 2009).  $\delta D_{fi}$  isotope ratios are given in per mil (‰) using the standard delta notation and are reported relative to the Vienna Standard Mean Ocean Water (VSMOW). We extracted 95 calcite blocks from 87 different depths, weighing between 1 and 1.5 g, from the central growth axis of stalagmite WB-21-5-A. Replicates were produced at 0.5, 10.5, 20.5, 30.5, and 40.5 cm depth. See (Dublyansky & Spötl, 2009) for details on the crushing procedure. The precision of replicate measurements of our in-house calcite standard is typically 1.5‰ for  $\delta D_{fi}$  for water amounts between 0.1 and 1  $\mu\text{l}$ . Because crushing of our calcite samples released up to 1  $\mu\text{l}$  of water (mean 0.40  $\mu\text{l}$ ), the precision of 1.5‰ for  $\delta D_{fi}$  was found to be adequate for this study. Temporal resolution is ~40 years.

The paleotemperature record of stalagmite WB-21-5-A was reconstructed based on the modern-day regional water isotope-temperature relationship (Rozanski et al., 1992). Only  $\delta D_{fi}$  values were used for calculating paleotemperatures for the following reasons: post-depositional processes can alter the original  $\delta^{18}\text{O}_{fi}$  in fluid inclusion water and thus limit the

use of  $\delta^{18}\text{O}_{\text{fi}}$  for paleotemperature calculations (McDermott, 2004). In addition,  $\delta\text{D}_{\text{fi}}$  is not affected by isotopic fractionation during calcite precipitation and remains unaltered as there is no hydrogen source once the water is entrapped in the calcite matrix. We used the global meteoric water line ( $\delta\text{D} = 8 * \delta^{18}\text{O} + 10\text{‰}$ ) to convert  $\delta\text{D}_{\text{fi}}$  to  $\delta^{18}\text{O}_{\text{calculated}}$ . Modern-day drip-water yielded a  $\delta^{18}\text{O}$  value of  $-10\text{‰}$  which was used as the modern-day  $\delta^{18}\text{O}$  anchor point. Fluid inclusion  $\delta^{18}\text{O}_{\text{calculated}}$  values were subtracted from this modern-day  $\delta^{18}\text{O}$  anchor point to obtain  $\delta^{18}\text{O}_{\text{difference}}$ . Next, a temperature- $\delta^{18}\text{O}$  transfer function (TF) was used to convert  $\delta^{18}\text{O}_{\text{difference}}$  into temperature. Because it is unclear which TF is appropriate, we evaluated a range of possible values, between 0.26 and 0.36 ‰/°C, which represents the error range of the south-central Alaska temperature- $\delta^{18}\text{O}$  slope of 0.31 ‰/°C (Bailey et al., 2019). Because there is a minor 0.1 °C difference in temperatures calculated from the range of TF values, we report temperatures based on the TF of 0.31 ‰/°C. Finally, we subtracted the mean annual temperature of a nearby weather Station in Klawock (55.555° N, 133.096° W; 24 m a.s.l. – Supplementary Fig. S2) of 7.4 °C (Western Regional Climate Center) to obtain paleotemperature anomaly values:

$$T = 7.4 - [-10 - \delta^{18}\text{O}_{\text{calculated}}] * \text{TF}. \quad (\text{Eq. 1})$$

A regional lapse rate likely causes cooler mean annual temperatures at the cave sites ~400 m higher in elevation, probably closer to the interior cave temperatures of Walkabout Cave (~5.6 °C) (Supplementary Fig. S4). In lieu of using unavailable long-term site-specific temperature data, we report temperature data as anomalies vs weather station Klawock (Fig. 4; Supplementary Fig. S6).

Uncertainties reflect isotope measurement errors, and one standard deviation of repeated measurements. The uncertainties are applied through all steps of the paleotemperature calculation. Further, uncertainties are propagated between sampling locations.

## Cave monitoring

HOBO Pro v2 temperature loggers (accuracy:  $\pm 0.21^{\circ}\text{C}$ ) were placed near the entrance of both Walkabout and Wishbone Caves, and near the extracted stalagmites. Temperature was measured at 1-hour intervals for 1 year, starting when the stalagmites were extracted (Supplementary Fig. S4).

A Stalagmate drip logger was placed directly where stalagmite WA-21-6-A was extracted, and recorded drip counts at 1-hour intervals for 1 year, starting when the stalagmite was extracted (Supplementary Fig. S4).

## Statistical analyses

For correlation estimation on two time series that are not observed on the same timescale, the ‘binned correlation coefficient’ (Mudelsee, 2014) is superior to interpolation because it does not introduce artificial serial dependence. This measure equals Pearson’s correlation coefficient calculated on the respective averages within time bins of the two-time series. The existence of persistence or ‘memory’ in a time series (which is typical for climate) on a particular grid of time values allows to infer the correlation with other time series that are observed on a different grid. The optimal binwidth for that procedure was obtained from the estimated persistence times using the software TAUEST (Mudelsee, 2002), the temporal spacings of the two series, and the binwidth formula after (Mudelsee, 2014), Eq. 7.48 therein. The uncertainty of the estimated binned correlation coefficients was determined by calibration of 90% Student’s  $t$  confidence intervals using the software PearsonT3 (Ólafsdóttir & Mudelsee, 2014), more than acceptable for geosciences. It should be noted that a confidence interval (for an estimation) is an uncertainty measure that is superior to a p-value (for a hypothesis test) because it carries more quantitative information. That means a confidence interval is for a statement about the strength of an association, not merely whether

there is one (Yates, 1951; Efron & Tibshirani, 1993). Furthermore, the suitability of this correlation method to climate data and its validity have been demonstrated by means of observed and artificial series (Mudelsee, 2014).

The spectra for the records were estimated on the detrended time series obtained with a Gasser–Müller nonparametric trend (Mudelsee, 2014) calculated with a bandwidth of 500 yr in order to exclude distortions from long-term variations. The spectral power was determined by means of the Lomb–Scargle Fourier transform combined with Welch’s overlapped segment averaging procedure (Mudelsee, 2014), which is implemented in REDFIT software (Schulz & Mudelsee, 2002). To determine a frequency-dependent correct factor for estimation bias stemming from the uneven spacings, we conducted 10,000 Monte Carlo simulations of an AR(1) red-noise process. Further spectrum estimation parameters (Schulz & Mudelsee, 2002) were: oversampling factor 64, highest-frequency factor 1.0, Welch I data taper, predefined equivalent autocorrelation coefficient (Schulz & Mudelsee, 2002; Mudelsee, 2008, 48) equal to 0.6632 (WA-21-6-A  $\delta^{18}\text{O}$ ; Fig. 2a) or 0.7909 (WB-21-5-A  $\delta^{18}\text{O}$ ; Fig. 2b), and number of segments equal to 17 (WA-21-6-A  $\delta^{18}\text{O}$ ) or 13 (WB-21-5-A  $\delta^{18}\text{O}$ ) in order to yield comparable 6-dB spectral resolution bandwidths for the two records. The significances of the spectral peaks were tested against the upper 99% level from the chi-squared distribution for the AR(1) alternative.

## References

- Ahn, J., *et al.* Atmospheric CO<sub>2</sub> over the last 1000 years: A high-resolution record from the West Antarctic Ice Sheet (WAIS) Divide ice core. *Global Biogeochem. Cycles* **26**, GB2027 (2012).
- Alexander, M.A., *et al.* The atmospheric bridge: The influence of ENSO teleconnections on air–sea interaction over the global oceans. *J. climate* **15**, 2205–2231 (2002).
- Allan, R.J. “ENSO and climatic variability in the past 150 years”, in *ENSO: Multiscale Variability and Global and Regional Impacts*. H. F. Diaz, V. Markgraf, Eds. (Cambridge Univ. Press, New York, 2000), pp. 3–55.
- Anderson, L., Abbott, M.B., Finney, B.P. & Burns, S.J. Regional atmospheric circulation change in the North Pacific during the Holocene inferred from lacustrine carbonate oxygen isotopes, Yukon Territory, Canada. *Quat. Res.* **64**, 21–35 (2005).
- Bailey, H.L., Klein, E.S. & Welker, J.M. Synoptic and mesoscale mechanisms drive winter precipitation  $\delta^{18}\text{O}/\delta^2\text{H}$  in south-central Alaska. *J. Geophys. Res.-Atmos.* **124**, 4252–4266 (2019).
- Bjerknes, J. A possible response of the atmospheric Hadley circulation to equatorial anomalies of ocean temperature. *Tellus* **18**, 820–829 (1966).
- Bjerknes, J. Atmospheric teleconnections from the equatorial Pacific. *Mon. Weather Rev.* **97**, 163–172 (1969).
- Bronk Ramsey, C. Deposition models for chronological records. *Quat. Sci. Rev.* **27**, 42–60 (2008).
- Bronk Ramsey, C. Bayesian analysis of radiocarbon dates. *Radiocarbon* **51**, 337–360 (2009).

360 Bronk Ramsey, C. & Lee, S. Recent and planned developments of the program OxCal.  
 361 *Radiocarbon* **55**, 720–730 (2013).

362 Büntgen, U., *et al.* Cooling and societal change during the Late Antique Little Ice Age from  
 363 536 to around 660 AD. *Nat. Geosci.* **9**, 231–236 (2016).

364 Clement, A.C., Seager, R., Cane, M.A., & Zebiak, S.E. An ocean dynamical thermostat. *J.*  
 365 *Climate* **9**, 2190–2196 (1996).

366 Cobb, K.M., Charles, C.D., Cheng, H. & Edwards, R.L. El Niño/Southern Oscillation and  
 367 tropical Pacific climate during the last millennium. *Nature* **424**, 271–276 (2003).

368 Cobb, K.M., *et al.* Highly variable El Niño–southern oscillation throughout the  
 369 Holocene. *Science* **339**, 67–70 (2013).

370 Cook, E.R., *et al.* Long-term aridity changes in the western United States. *Science* **306**, 1015–  
 371 1018 (2004).

372 Dansgaard, W. Stable isotopes in precipitation. *Tellus* **16**, 436–468 (1964).

373 Dee, S.G. *et al.* No consistent ENSO response to volcanic forcing over the last  
 374 millennium. *Science* **367**, 1477–1481 (2020).

375 Deser, C., Alexander, M.A., Xie, S.P. & Phillips, A.S. Sea surface temperature variability:  
 376 Patterns and mechanisms. *Annu. Rev. Mar. Sci.* **2**, 115–143 (2010).

377 Diaz, H.F., Hoerling, M.P. & Eischeid, J.K. ENSO variability, teleconnections and climate  
 378 change. *Int. J. Climatol.* **21**, 1845–1862 (2001).

379 Dublyansky, Y.V. & Spötl, C. Hydrogen and oxygen isotopes of water from inclusions in  
 380 minerals: design of a new crushing system and on-line continuous-flow isotope ratio  
 381 mass spectrometric analysis. *Rapid Commun. Mass Spectrom.* **23**, 2605–2613 (2009).



382 Efron, B., Tibshirani, R.J. (1993) An Introduction to the Bootstrap. Chapman and Hall, New  
383 York, 436 pp.

384 Emile-Geay, J., Cane, M., Seager, R., Kaplan, A. & Almasi, P. El Niño as a mediator of the  
385 solar influence on climate. *Paleoceanography* **22**, PA3210 (2007).

386 Freund, M.B., *et al.* Higher frequency of Central Pacific El Niño events in recent decades  
387 relative to past centuries. *Nat. Geosci.* **12**, 450–455 (2019).

388 Giamalaki, K., *et al.* Signatures of the 1976–1977 regime shift in the North Pacific revealed  
389 by statistical analysis. *J. Geophys. Res.-Oceans* **123**, 4388–4397 (2018).

390 Graham, N.E. Decadal-scale climate variability in the tropical and North Pacific during the  
391 1970s and 1980s: Observations and model results. *Clim. Dyn.* **10**, 135–162 (1994).

392 Hare, S.R. & Mantua, N.J. Empirical evidence for North Pacific regime shifts in 1977 and  
393 1989. *Prog. Oceanogr.* **47**, 103–145 (2000).

394 Hendy, C.H. The isotopic geochemistry of speleothems—I. The calculation of the effects of  
395 different modes of formation on the isotopic composition of speleothems and their  
396 applicability as palaeoclimatic indicators. *Geochim. Cosmochim. Acta* **35**, 801–824  
397 (1971).

398 Liu, Z. & Alexander, M. Atmospheric bridge, oceanic tunnel, and global climatic  
399 teleconnections. *Rev. Geophys.* **45**, RG2005 (2007).

400 Ólafsdóttir, K.B. & Mudelsee, M. More accurate, calibrated bootstrap confidence intervals  
401 for estimating the correlation between two time series. *Math. Geosci.* **46**, 411–427  
402 (2014).

403 Osterberg, E.C., *et al.* Mount Logan ice core record of tropical and solar influences on  
 404 Aleutian Low variability: 500–1998 AD. *Journal of Geophysical Research:*  
 405 *Atmospheres* **119**, 11–189 (2014).

406 Mann, M.E., *et al.* Global signatures and dynamical origins of the Little Ice Age and  
 407 Medieval Climate Anomaly. *Science* **326**, 1256–1260 (2009).

408 Mayo, L.R. & March, R.S. Air temperature and precipitation at Wolverine Glacier, Alaska;  
 409 Glacier growth in a warmer, wetter climate. *Ann. Glaciol.* **14**, 191–194 (1990).

410 McDermott, F. Palaeo-climate reconstruction from stable isotope variations in speleothems: a  
 411 review. *Quat. Sci. Rev.* **23**, 901–918 (2004).

412 McPhaden, M.J., Zebiak, S.E. & Glantz, M.H. ENSO as an integrating concept in Earth  
 413 Science. *Science* **314**, 1740–1745 (2006).

414 Moussas, X., Polygiannakis, J.M., Preka-Papadema, P. & Exarhos, G. Solar cycles: A  
 415 tutorial. *Adv. Space Res.* **35**, 725–738 (2005).

416 Mudelsee, M. TAUEST: A computer program for estimating persistence in unevenly spaced  
 417 weather/climate time series. *Comput. Geosci.* **28**, 69–72 (2002).

418 Mudelsee, M. *Climate Time Series Analysis: Classical Statistical and Bootstrap Methods*,  
 419 *2nd edition* (Springer, Cham, Switzerland, 2014). [Atmospheric and Oceanographic  
 420 Sciences Library]

421 Rozanski, K., Araguas-Araguas, L. & Gonfiantini, R. Relation between long-term trends of  
 422 oxygen-18 isotope composition of precipitation and climate. *Science* **258**, 981–985  
 423 (1992).

424 Rubino, M., *et al.* Revised records of atmospheric trace gases CO<sub>2</sub>, CH<sub>4</sub>, N<sub>2</sub>O, and  $\delta^{13}\text{C}$ -CO<sub>2</sub>  
425 over the last 2000 years from Law Dome, Antarctica. *Earth Syst. Sci. Data* **11**, 473–  
426 492 (2019).

427 Schulz, M. & Mudelsee, M. REDFIT: Estimating red-noise spectra directly from unevenly  
428 spaced paleoclimatic time series. *Comput. Geosci.* **28**, 421–426 (2002).

429 Shen, C.C., *et al.* High-precision and high-resolution carbonate <sup>230</sup>Th dating by MC-ICP-MS  
430 with SEM protocols. *Geochim. Cosmochim. Acta* **99**, 71–86 (2012).

431 Sigl, M., *et al.* Timing and climate forcing of volcanic eruptions for the past 2,500  
432 years. *Nature* **523**, 543–549 (2015).

433 Spötl, C. Long-term performance of the Gasbench isotope ratio mass spectrometry system for  
434 the stable isotope analysis of carbonate microsamples. *Rapid Commun. Mass*  
435 *Spectrom.* **25**, 1683–1685 (2011).

436 Stevenson, S., *et al.* Will there be a significant change to El Niño in the twenty-first  
437 century? *J. Climate* **25**, 2129–2145 (2012).

438 Takahashi, T., Sutherland, S.C., Wanninkhof, R., *et al.* Climatological mean and decadal  
439 change in surface ocean pCO<sub>2</sub>, and net sea–air CO<sub>2</sub> flux over the global oceans. *Deep*  
440 *Sea Res. Part II: Top. Stud. Oceanogr.* **56**, 554–577 (2009).

441 Vecchi, G.A., Clement, A. & Soden, B.J. Examining the tropical Pacific's response to global  
442 warming. *Eos* **89**, 81–83 (2008).

443 Wang, B., *et al.* Historical change of El Niño properties sheds light on future changes of  
444 extreme El Niño. *Proc. Natl. Acad. Sci.* **116**, 22512–22517 (2019).

445 Western Regional Climate Center, “Klawock climate summary” ([wrcc.dri.edu/](http://wrcc.dri.edu/)).

446 Wilcox, P.S., *et al.* Millennial-scale glacial climate variability in Southeastern Alaska follows  
447 Dansgaard-Oeschger cyclicity. *Sci. Rep.* **9**, 1–8 (2019).

448 Wiles, G.C., Barclay, D.J., Calkin, P.E. & Lowell, T.V. Century to millennial-scale  
449 temperature variations for the last two thousand years indicated from glacial geologic  
450 records of Southern Alaska. *Global Planet. Change* **60**, 115–125 (2008).

451 Wu, C.J., Krivova, N.A., Solanki, S.K. & Usoskin, I.G. Solar total and spectral irradiance  
452 reconstruction over the last 9000 years. *Astron. Astrophys.* **620**, A120 (2018).

453 Yates, F. The influence of Statistical Methods for Research Workers on the development of  
454 the science of statistics. *J. Am. Stat. Assoc.* **46**, 19–34 (1951).

455

456

457

458

459

460

461

462

463

464

465

466

467

468 **Acknowledgments:** We are grateful for the Jim Baichtal, Anna Harris, and the Tongass  
469 National Forest Geology program for their continued support for this work. Additionally,  
470 extensive stable isotope sampling used in this manuscript was conducted by Jessica  
471 Honkonen.

472 **Funding:** This work was funded by the Austrian Science Fund (FWF) grant FP338960 to  
473 P.S.W.

474 **Author contributions:**

475 Conceptualized: P.S.W.

476 Funding acquisition: P.S.W.

477 Administered/supervised the project: P.S.W.

478 Methodology design: P.S.W.

479 Conducted the U-Th and fluid inclusion analysis: P.S.W.

480 Prepared visual components: P.S.W., M.M.

481 Writing—original draft: P.S.W.

482 Writing—reviewing and editing: M.M., C.S., R.L.E.

483 Conducted the formal analyses of the data: M.M.

484 Provided resources necessary for the analytical sampling: C.S., R.L.E.

485 **Competing interests:** There are no competing interests.

486 **Data and materials availability:** U-Th, Fluid inclusion, and stable isotope data can be found  
487 at: <https://doi.pangaea.de/10.1594/PANGAEA.949778>.

488 **Supplementary Materials:** Supplementary Figs. S1 – 12

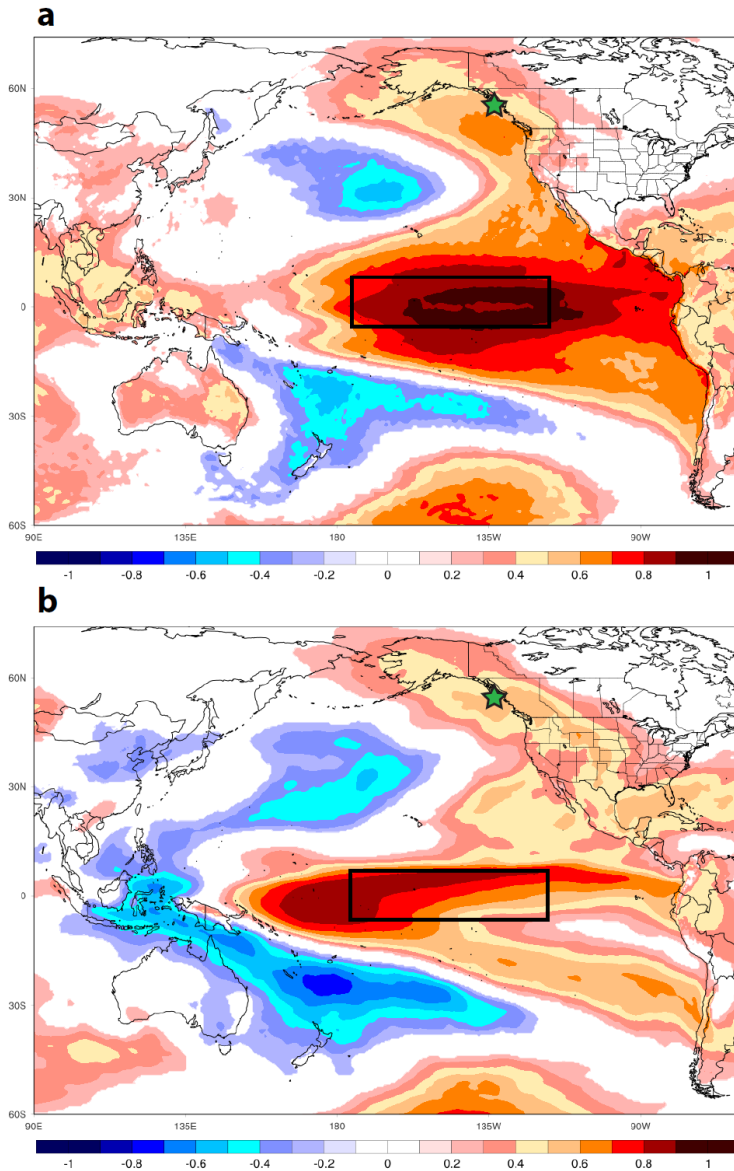


Fig. 1: Spatial correlation of ERA5 Reanalysis 2 m temperature (a) and precipitable water (b) with the Niño 3.4 index. Regions of significant correlation are highlighted by color bands (Pearson's correlation [90% CI]). Black box indicates NINO3.4 region, while the speleothem sample location of this study is marked by the green star. Refer to Supplementary Fig. S2 for a more detailed map of the study area. This plot was generated using Climate Reanalyzer (<http://cci-reanalyzer.org>), Climate Change Institute, University of Maine, USA.

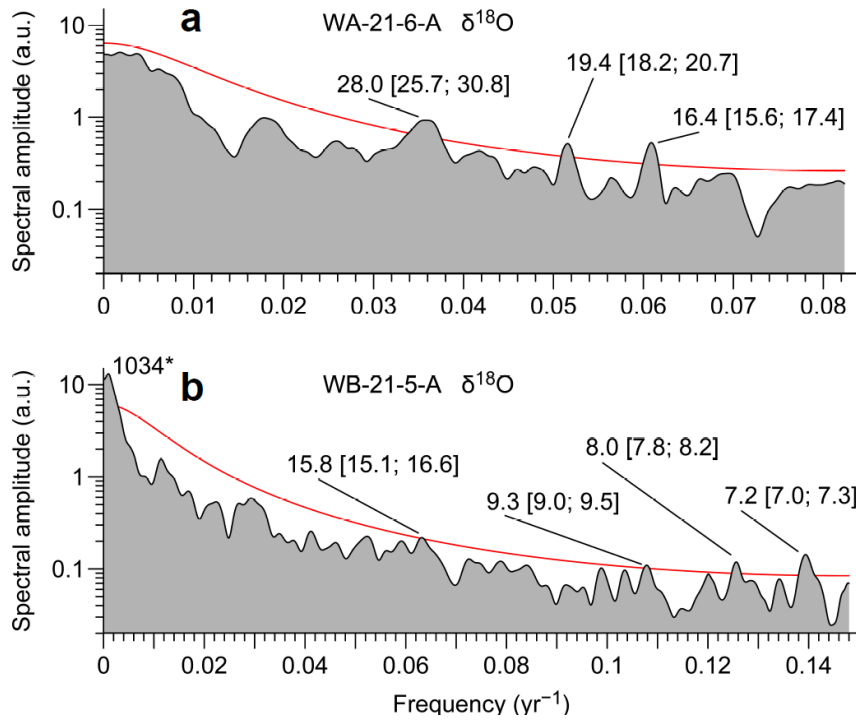
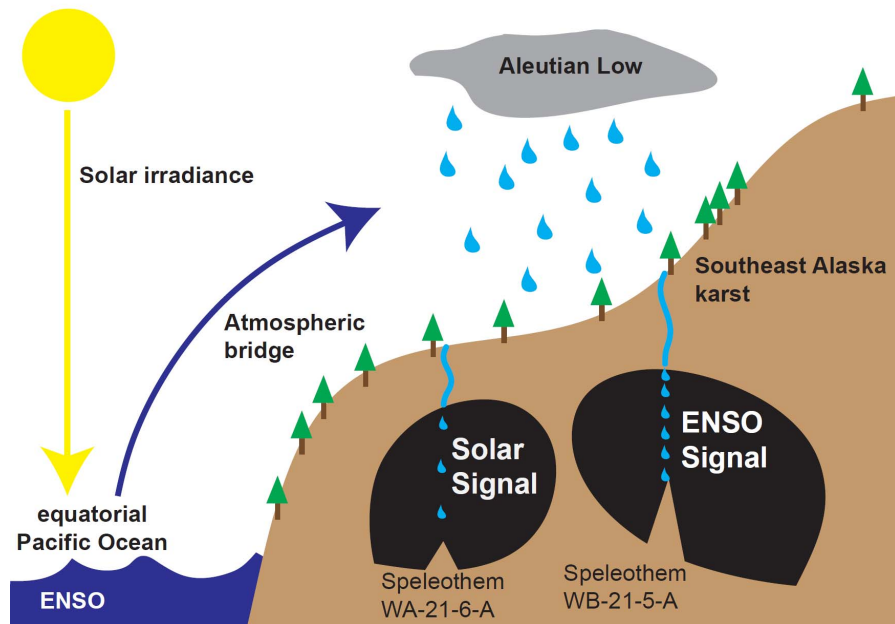


Fig. 2: Spectral analysis results for  $\delta^{18}\text{O}$  records from speleothems WA-21-6-A (a) and WB-21-5-A (b). Where spectrum estimate (shaded) exceeds the upper 99% level of the red-noise alternative (red line), peaks are labelled with period value and  $\pm$  bandwidth interval (both in yr); a.u., arbitrary units; asterisk denotes uncertain peak, likely due to incompletely removed nonlinear trend. Note logarithmic y-axes.



508

509 Fig. 3: Schematic illustrating how the Aleutian Low is forced by both solar irradiance and  
 510 ENSO through the atmospheric bridge. The epikarst is effective at filtering the regional  
 511 Aleutian Low climate into either the solar irradiance or ENSO signals.



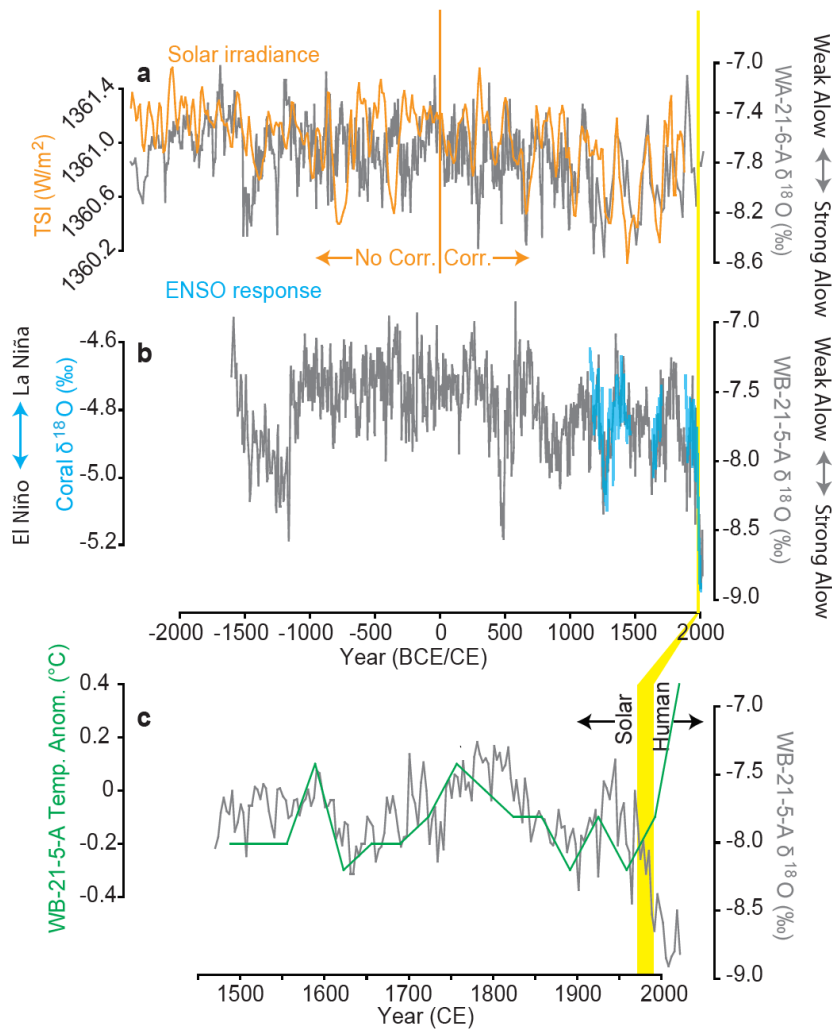


Fig. 4: Southeastern Alaska speleothem record compared with solar irradiance and ENSO proxy data. **a** Speleothem WA-21-6-A  $\delta^{18}\text{O}$  vs total solar irradiance (TSI) (Wu et al., 2018). Orange line denotes timing of correlation differences between TSI and WA-21-6-A, with significant correlation after 0 CE and no significant correlation before 0 CE; **b** Speleothem WB-21-5-A  $\delta^{18}\text{O}$  vs coral  $\delta^{18}\text{O}$  (Dee et al., 2020). Alow = Aleutian Low; **c** Magnified time interval comparing speleothem WB-21-5-A  $\delta^{18}\text{O}$  and temperature anomalies. Refer to Supplementary Fig. S6 for an extended temperature plot. In **a**, **b**, **c**, yellow bar highlights North Pacific regime shift, when ENSO is disconnected from solar forcing and anthropogenic forcing takes over.